

# **The VIMS Wavelength and Radiometric Calibration 19, Final Report**

Roger N. Clark<sup>1</sup>, Robert H. Brown<sup>2</sup>, Dyer M. Lytle<sup>2</sup>, Matt Hedman<sup>3</sup>

<sup>1</sup> Planetary Science Institute, Lakewood, CO, 80227

<sup>2</sup> Department of Planetary Sciences, University of Arizona, Tucson, AZ, 85721

<sup>3</sup> University of Idaho, Moscow, Idaho

NASA Planetary Data System

Version 2.0

01/25/2018

Clark, R. N., R. H. Brown, D. M. Lytle, Hedman, M., 2018, The VIMS Wavelength and Radiometric Calibration 19, Final Report, *NASA Planetary Data System*, The Planetary Atmospheres Node, 30p. [http://atmos.nmsu.edu/data\\_and\\_services/atmospheres\\_data/Cassini/vims.html](http://atmos.nmsu.edu/data_and_services/atmospheres_data/Cassini/vims.html)

## **Abstract**

We derive the final radiometric calibration of the mission for the Visual and Infrared Mapping Spectrometer (VIMS) on Cassini. The VIMS instrument has undergone shifts in the wavelength calibration of the spectrometer after launch, with large shifts during the Jupiter fly-by in 2000, a period of stability until Saturn orbit insertion, then small shifts throughout the orbital tour until the end of mission in September, 2017. We adopt a “zero point” shift as the quiet period from 2002.9 to 2005.0, which we call the standard wavelengths. The maximum shift during the Saturn orbital tour was 9.8 nm (0.59 channels). Before the Jupiter encounter, the wavelengths relative to the standard were at -25.8 nm (-1.55 channels) with large shifts through the Jupiter flyby. The wavelength shifts require a time-dependent radiometric calibration technique to be deployed to preserve radiometric accuracy. Herein we quantify the time-dependent wavelength shift, and describe a compensatory scheme that provides an accurate calibration for both specific intensity and I/F for VIMS measurements made during the Cassini Mission. We also discuss unresolved issues.

## Introduction

The radiometric responsivity of a spectrometer or imaging instrument is complex, depending upon many factors, some of the most important being the aperture collection area, spectral transmission of the optical system, and the response function of the detector(s). The VIMS is an imaging spectrometer (Miller *et al.*, 1996, Brown *et al.*, 2004) whose spectral responsivity varies with angular position in the field of view and with wavelength. The IR channel primary optical design incorporates Ritchey Cretien foreoptics, a reverse-Dahl-Kirkham collimator with a large central obscuration, a triply blazed reflection grating, Cassegrain camera optics and a linear, 256-element array of InSb detectors overlain with 4 order-sorting/thermal-blocking filter segments. The VIS channel uses an off-axis Shafer telescope with an Offner design spectrometer. The flat-field response of the instrument varies with wavelength, and a flat-field image cube with 352 wavelengths is thus employed to correct the system response over the field of view relative to the instrument's boresight pixel. The spectral bandpass of the instrument also varies slightly across the full range of VIMS' spectral response, adding to the complexity of the calibration. Additional issues arise due to ringing in the instrument response function driven primarily by the blocking/order-sorting filters on the VIMS focal plane (in some cases  $\pm 10\%$  or more [Figure 1]). Because of the ongoing wavelength shifts in the instrument, relative to when the instrument response function was measured on the ground and after the Cassini Jupiter flyby in late 2000, artifacts in radiometrically calibrated spectra result because the response function at any later time is actually sampled at different wavelengths than the wavelength set used in the ground measurements. The resulting artifacts are primarily caused by the use of a response function in multiplicative or divisive operations sampled using the original, ground wavelength set. When used to calibrate to specific intensity or I/F instrument data obtained at a later time would be done with a different set of wavelengths than derived from the ground calibration. Below we describe our methodology to track the shifting wavelengths, and then apply a time-dependent, radiometric calibration that compensates for all the known effects.

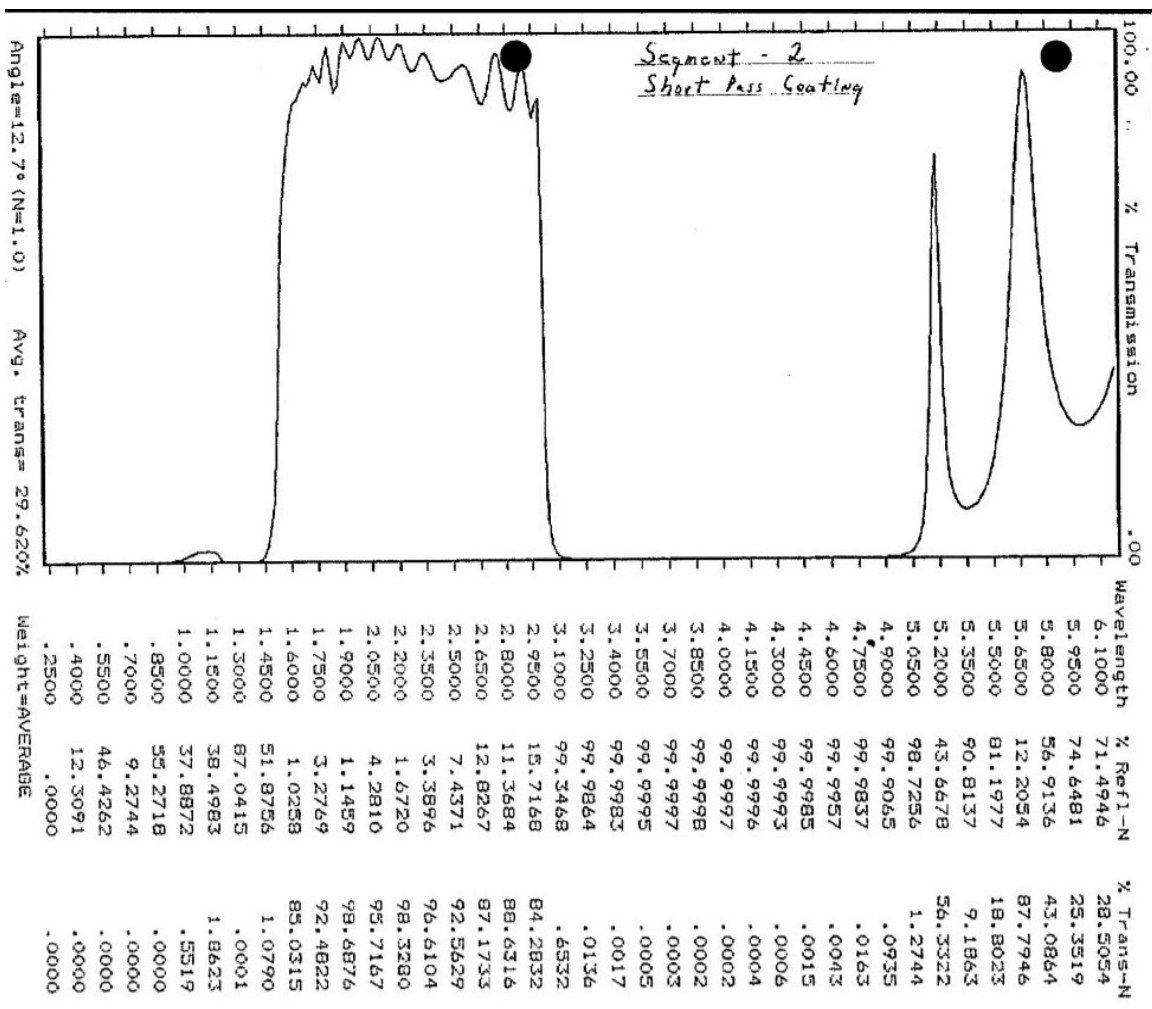


**Figure 1.** VIMS order-sorting/blocking filter transmission for the 1.6-3.0 micron segment. The ringing in the transmission propagates into the radiometric calibration in a complex way because a shift in wavelength samples different places in the response function. (From Al-Jumaily, 1991).

## VIMS Wavelengths Versus Time

The VIMS calibration pipeline and PDS-delivered data used a wavelength set and FWHM set measured during thermal vacuum testing at JPL before launch (Brown *et al.*, 2004), but shifted by 1.3 channels as observed in Galilean Satellite data obtained during the Jupiter flyby (McCord *et al.*, 2001). The calibration also incorporated a small, additional set of corrections to a few channels near the wavelength of the 4.25 micron CO<sub>2</sub> absorption (Cruikshank *et al.*, 2010). Here we employ terminology to describe the various corrections to the VIMS Radiometric Calibrations by using a numbering scheme RCnn (Radiometric Calibration nn). RC17 was the primary calibration used until June, 2016 (Clark *et al.*, 2012), and has been used in all data processed through the VIMS calibration pipeline, and all calibration files delivered to the PDS prior to the calibration RC19 described herein. Calibration RC19 was put in place in the VIMS pipeline in June 2016 with projections to the end of mission (Clark *et al.*, 2016). In this paper we use data through the end of mission and include for the first time analysis of the wavelength shifts back to before the Jupiter encounter.

The wavelength shift of the instrument since Cassini's Saturn Orbit Insertion (SOI) is the reason why we employ a time-dependent radiometric calibration. It has been intensively studied since about 2013. Two methods for determining the VIMS wavelengths have been employed. (1) Monitoring, as a function of time, the reflectivity in 3 windows of the Titan spectrum (1.6, 2.0, 2.8 microns) by fitting Gaussian profiles to the window peaks. (2) Using the VIMS internal, wavelength-calibration, laser diode (central wavelength ~0.979 microns), and employing a fit to the Gaussian intensity profile of the calibration diode convolved with the response of 8 VIMS channels centered near peak intensity of the calibration diode. The result is the derivation of a time-dependent shift of the current wavelengths relative to the set extant at the time of Cassini's SOI. Figures 2a, 2b, and 2c show the results from both methods.

To determine the absolute wavelength calibration of the VIMS infrared instrument before Saturn orbit insertion back to the Jupiter flyby, a combination of calibration-diode measurements, and spectra of Jupiter before, during and after the Jupiter flyby were used. Spectra of Jupiter were used to determine relative wavelength shifts during the cruise phase that encompassed the Jupiter flyby. Those relative shifts were subsequently put on an absolute scale by using spectra of Jupiter obtained in 2016, day 262 while in Saturn orbit, observation VIMS\_242JU\_FULLDISK001. The absolute wavelength position of the averaged VIMS spectra of Jupiter from the 2016 observations, calibrated with contemporary results from the VIMS calibration diode, were then compared to the relative wavelength shifts derived from spectra from the Jupiter flyby using a least-squares technique to shift the spectra to best match the absorption bands in Jupiter's spectrum. Results are illustrated in Figure 3.

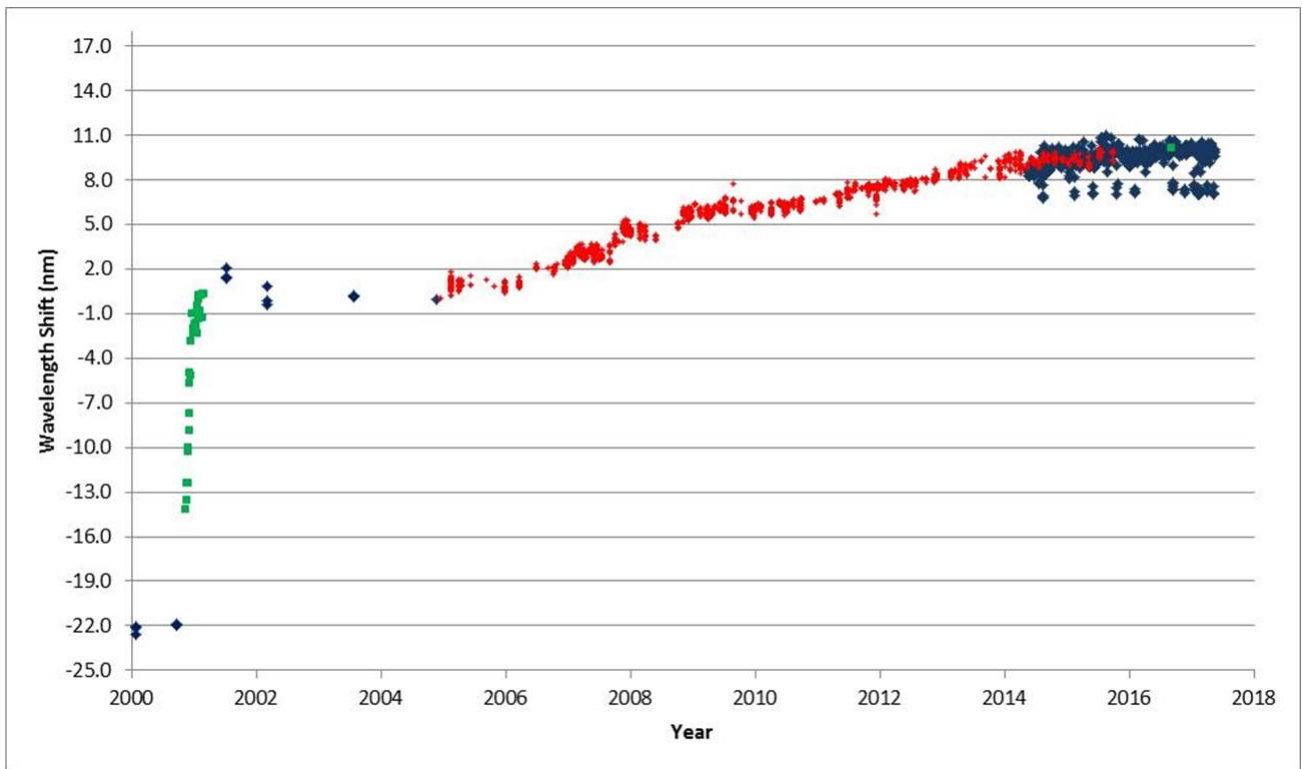


**Figure 2a.** VIMS wavelength shift versus time for three methods: Titan atmospheric windows (red points), Jupiter atmospheric windows (green points) and VIMS calibration diode (dark blue points). The lone green point near 2017 is the Jupiter reference spectrum, measured while in Saturn orbit, and was used to fit Jupiter VIMS data to determine absolute wavelengths during the Jupiter flyby.

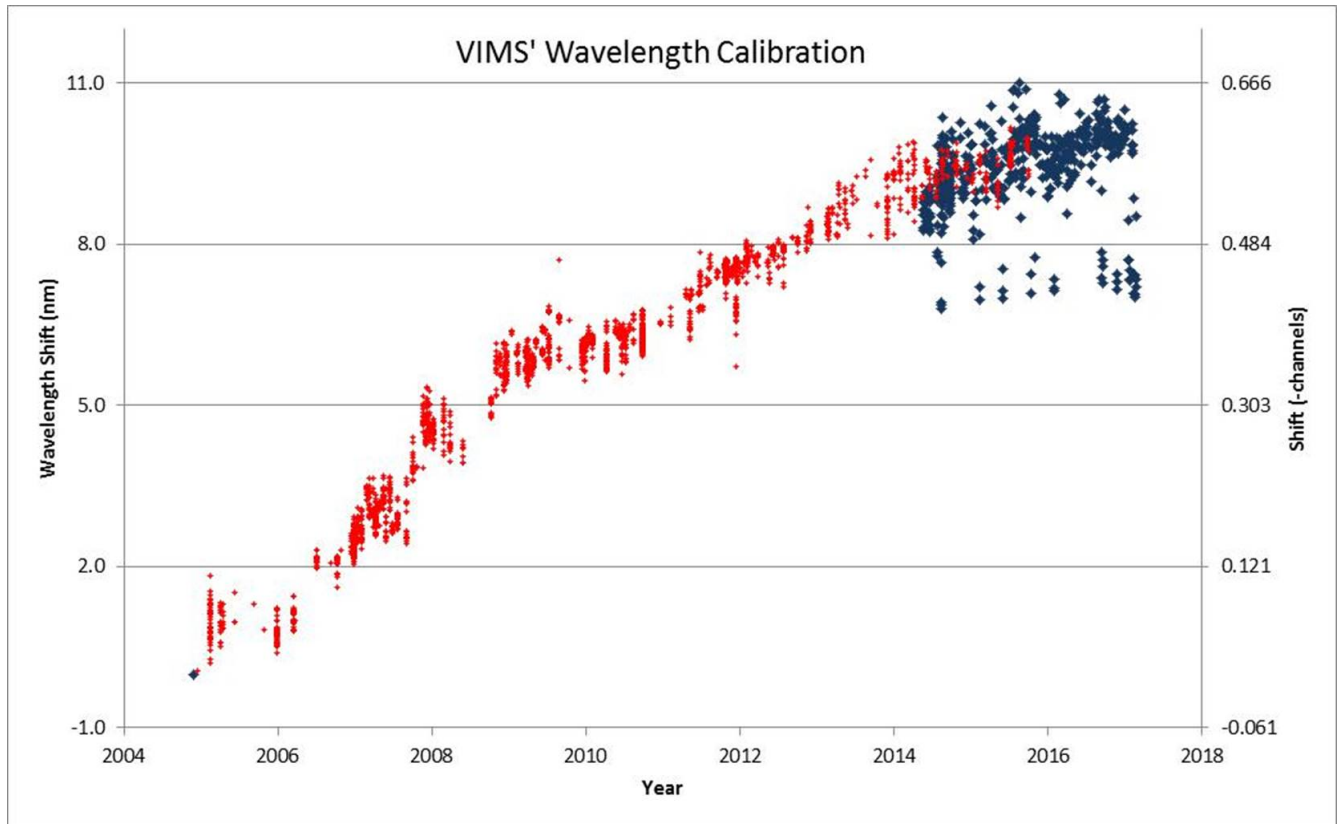


**Figure 2b.** VIMS wavelength shift versus time. The large deviations toward shorter wavelengths in the calibration diode measurements are due to transient thermal fluctuations in the VIMS IR spectrometer optics driven by changes in spacecraft orientation during particular observations in the orbital tour. Similar fluctuations show in the shifts derived using Titan data, but they are of much smaller magnitude because the Titan data integrate over larger time spans where the VIMS spectrometer temperature is closer to nominal. It is also the case that spacecraft orientation during most Titan flybys where the optical remote sensing instruments were prime was less prone to heating the VIMS spectrometer optics. These data are the same data as in Figure 2a, showing the shifts during the Saturn orbital tour.

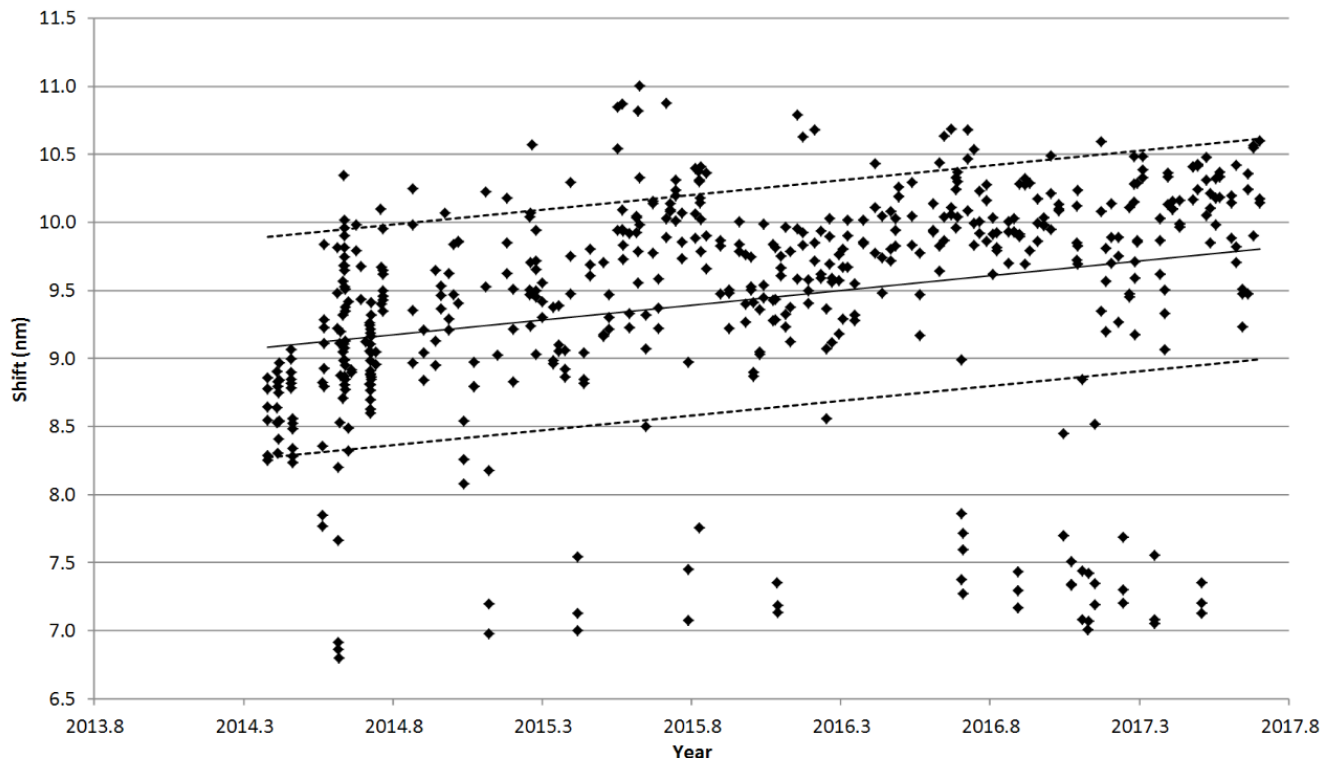


**Figure 2c.** VIMS wavelength shift as measured by the calibration diode. The central, solid line is a linear regression, and the two dotted lines are  $\pm 1$  sigma as measured relative to the linear fit. The outlier points indicate real short term variations, most likely caused by temperature cycling of the VIMS spectrometer optics.

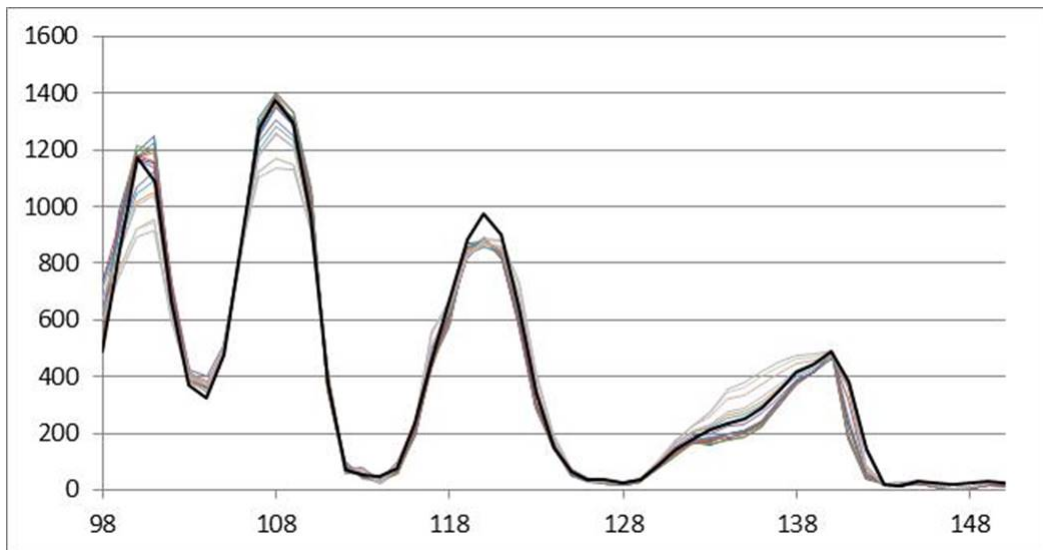


**Figure 3.** Illustration of alignment agreement of the Jupiter fly-by data after applying the shifts in Figure 2a. The horizontal axis is VIMS channel number.

We specify the shift as a function of time in Table 1, and generate a new wavelength set with the associated calibration files when the change in wavelength relative to the previous period would be 0.5 nm (about 1/30th of one channel). The shifts are relative to the new “standard 2004.0” wavelengths given in Table 2.

## Calibration Equations

The basic equation we employ for calibrated, specific intensity,  $I$ , at one wavelength is:

$$(1) \quad I = \frac{(R_{DN} - Dark)}{flat} CB,$$

where  $R_{DN}$  is the instrument raw data number in a given exposure,  $Dark$  is the instrument measured dark current and thermal background (a dark/thermal background measurement is made after every VIMS scan line using the same exposure time with the shutter closed), and  $flat$  is the VIMS flat-field response at the given wavelength and position within the field of view normalized to the response of the boresight pixel (i.e., the relative response of the boresight pixel in the flat-field cube is 1 at every wavelength). The units of equation 1 are: energy/time/area/bandpass/solid angle.

$C$  is defined as the calibration-multiplier vector which includes system transmission, grating efficiency, detector response, and divided by the exposure time (see equations 4a and 4b, below).

$$(2) \quad B = \frac{h c}{\lambda A \Omega \Delta\lambda},$$

where

$\lambda$  = wavelength,

$\Delta\lambda$  = full width, half maximum, FWHM,

$\Omega$  = solid angle =  $2.5 \times 10^{-7}$  steradian,

$A$  = aperture area IR:  $A = 96.1 \text{ cm}^2 = 0.00961 \text{ m}^2$ , VIS:  $A = 15.88 \text{ cm}^2$ ,  $A = 0.001588 \text{ m}^2$ ,

$c$  = speed of light =  $2.998 \times 10^{10} \text{ cm/s} = 2.998 \times 10^8 \text{ m/s}$ , and

$h$  = Planck constant =  $6.626 \times 10^{-27} \text{ erg-s} = 6.626 \times 10^{-34} \text{ J-s} (= \text{W s}^2)$ .

The calibration to apparent reflectance,  $I/F$ , referred to that of a Lambert disk (a perfect diffuse reflector) is (note that the factor of  $\pi$  comes from the result that  $I/F$  for a Lambert disk is  $\pi^{-1}$ ):

$$(3) \quad \frac{I}{F} = \pi \frac{(R_{DN} - Dark)}{flat} \times \frac{CB}{S},$$

where  $t$  is the exposure time – 0.004 second for the IR, or just the exposure time in seconds for the VIS channel, and  $S$  is the solar spectrum from Thompson *et al.* (2015), corrected to the flux extant at the heliocentric distance of the object in question. The 4 millisecond IR exposure time correction is due to settling time after each mirror movement of the scanning secondary and was derived by McCord *et al.*, (2004).

In the VIMS instrument,  $A$  and  $\Omega$  are more complex (see Brown *et al.*, 2005). In standard resolution

mode, the VIS channel bins 3x3 pixels to make a 0.5 x 0.5 mradian IFOV, and the IR IFOV is actually 0.5 x 0.25 mradian which gets moved 0.25 mradian half way through the integration to make a 0.5 x 0.5 mradian square pixel. In high resolution mode, the VIS channel is 0.17 x 0.17 and the IR is 0.5 x 0.25 mradian. The full telescope aperture, a 22.9 cm diameter Ritchey-Cretien telescope, 800-mm focal length, has obscuration in both the Ritchey-Cretien secondary, and in the inverse Dahl-Kirkham collimator and Cassegrain spectrometer optics. We use different constants to scale the relative multiplier (equation 4, below) to compensate for these factors to derive the value of C for each VIS and IR channel and each wavelength.

### **Derived Spectral Properties**

The wavelength calibration and FWHM for VIMS were measured on the ground in a thermal vacuum chamber before launch (Brown *et al.*, 2005). At the Jupiter fly-by it was determined that the IR wavelengths had shifted 1.3 channels from the ground calibration (McCord *et al.*, 2001). That 1.3-channel shift from the ground calibration defined the VIMS standard wavelengths for post launch to RC17. We now know that the 1.3-channel shift was more complex (Figure 2a).

Using the measured wavelength shifts from Table 1 we modeled the effect of the shift on solar port data from 2005 to 2012 (Figure 4). The model does not include order-sorting/blocking-filter response. Unfortunately, as the data in Figure 1 show, the analog plot of filter transmission made over 20 years ago is not precise enough for tracking the effects of the wavelength shifts.

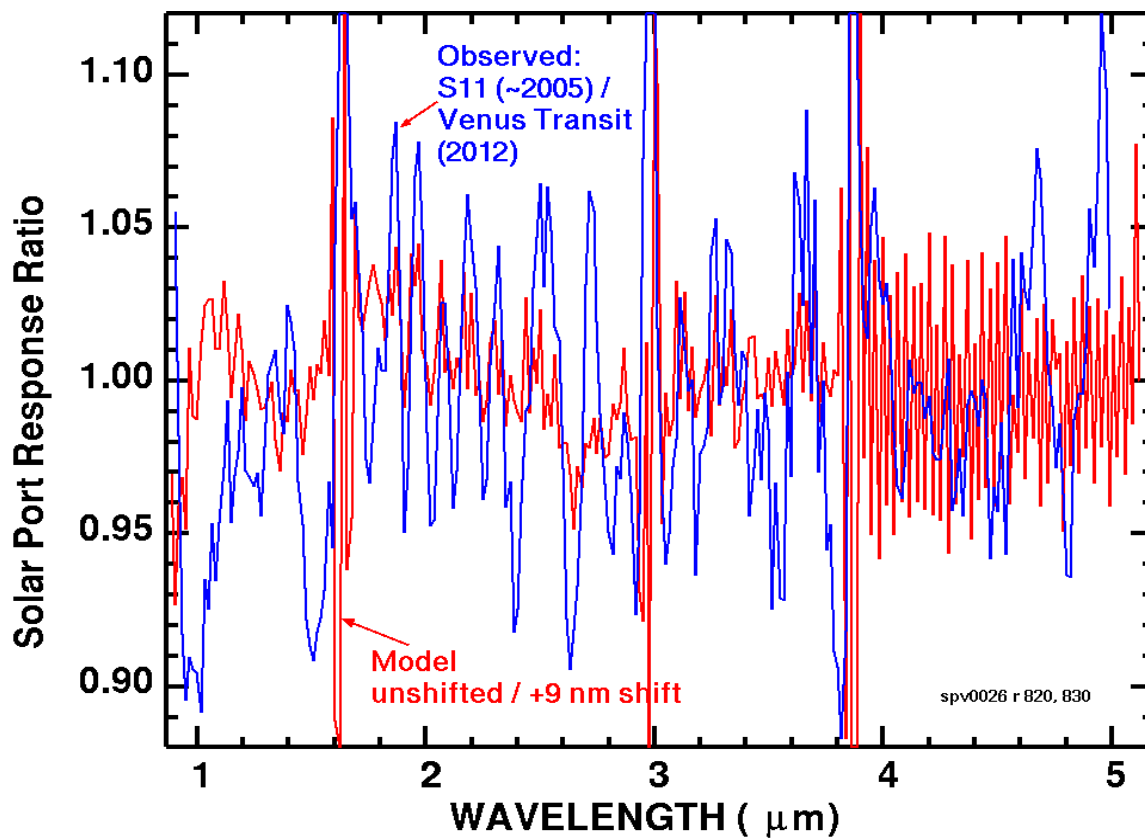


**Figure 4.** Solar port data from 2005 divided by data from 2012 (blue line) shows larger than predicted changes than just due to solar spectral structure.

Investigation of the causes of the discrepancy shown in Figure 4 revealed that, besides ringing in the order sorting filter transmission, fine structure in the original measured wavelengths of each vims channel and the derived FWHM display periodic structure which we traced to a periodic error in the grating position of the test monochromator used in the ground-based, thermal-vacuum testing of VIMS. Figures 5 and 6 show the trends.

```
VIMS Waves (um)3/2009/trend cspline      file= v      939 (spv0029 )
history=f12:interpolate using spv0029  rec  937 + waves, see manhst
1.005
```

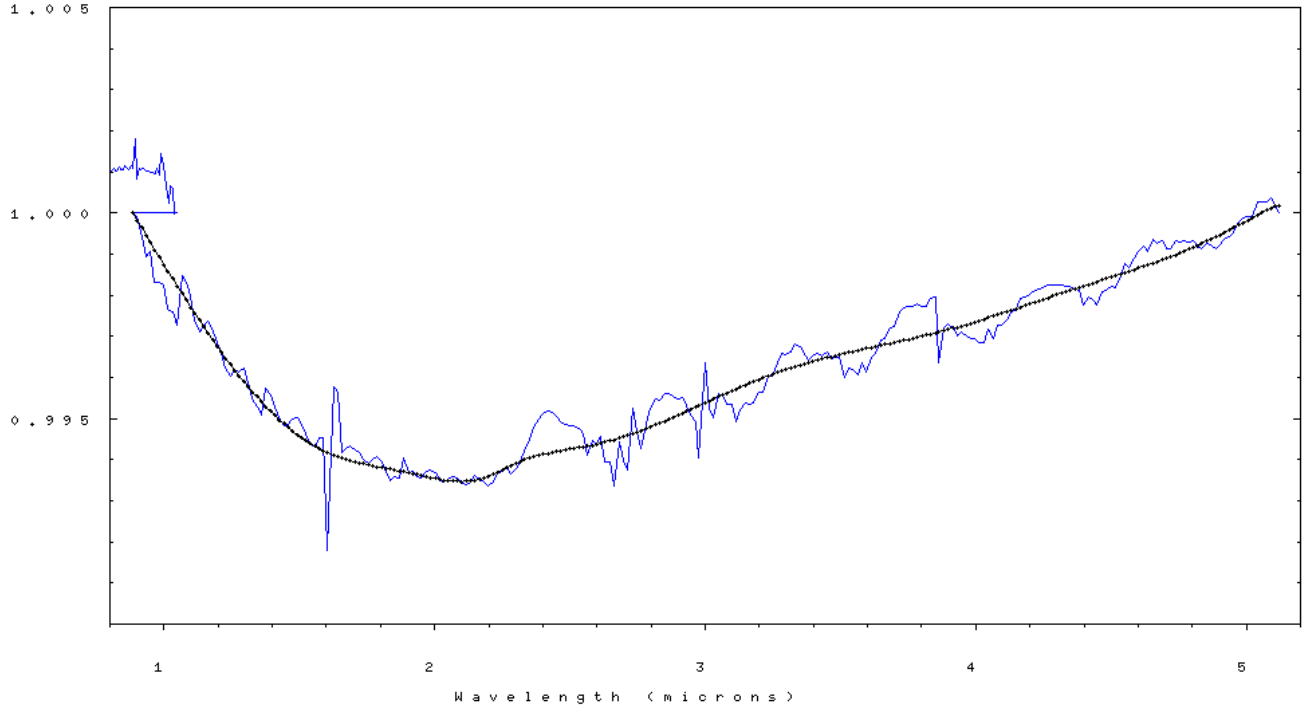


**Figure 5.** VIMS IR wavelengths divided by a linear fit to the end channels of the IR spectrometer (blue line). A cubic-spline fit (black line) is our new derivation: the new RC19 2004.0 “standard” wavelength set (values in Table 2). The blue line is a plot of the wavelengths derived in thermal vacuum testing before launch and shifted 1.3 channels (derived that the Jupiter fly-by pre RC19) with a correction for the wavelengths around the 4.25 micron CO<sub>2</sub> atmospheric absorption (Cruikshank *et al.* 2010).

```
Cassini VIMS Vis+IR resol um 352ch v2se1 file= v 933 (spv0029 )
history= f14: edited file spv0029 929
```

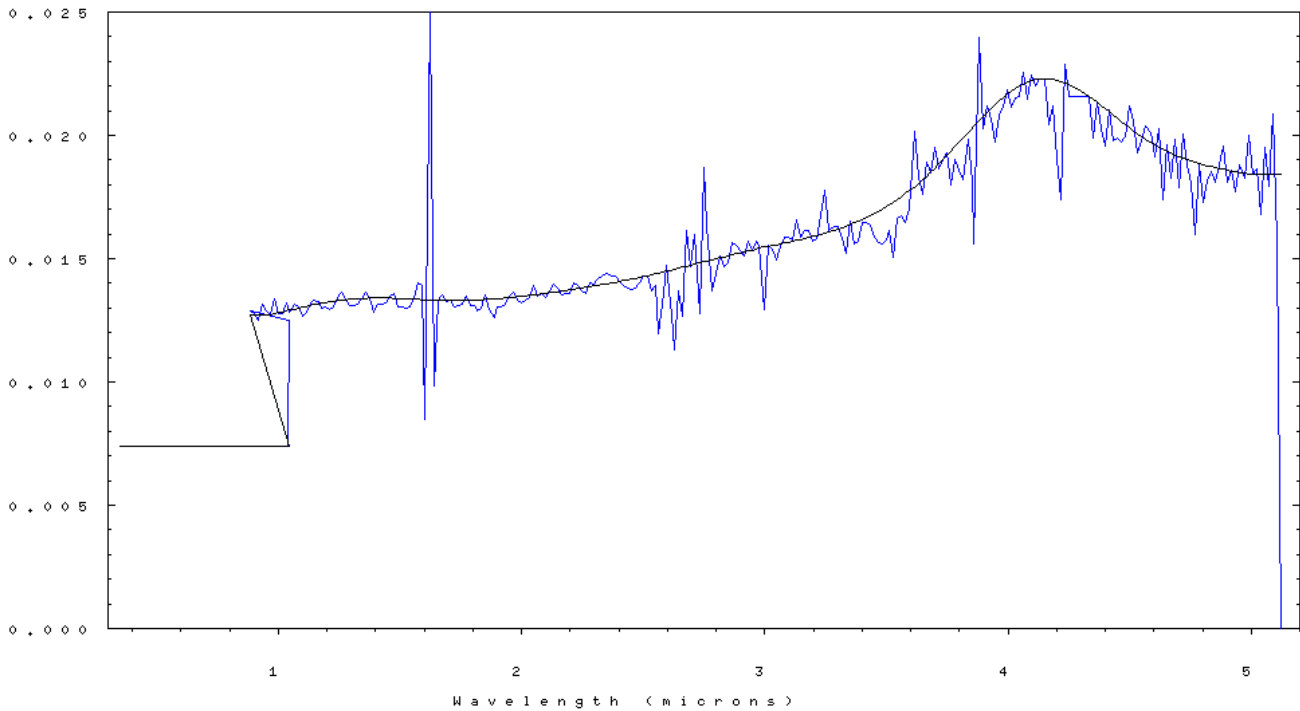


**Figure 6.** VIMS IR-channel bandpasses (FWHM) in microns (blue line) derived during thermal vacuum testing before launch. A cubic-spline fit (black line) defines the new RC19 FWHM set (values in Table 2).

## Calibration Multiplier

The calibration multiplier vector,  $C$ , from equation 1 is the major factor that remains to be determined. Ideally it could be derived from measurements of a known, standard reflector illuminated with a source of known intensity, such as a calibration target on the spacecraft illuminated by the Sun, but such a device was descope'd from VIMS in early Cassini budget cuts, thus we are left with only more approximate methods. Standard stars (that is, stars whose spectral specific intensities are known with the required precision) could be used, but because they are sub-pixel to VIMS, and because the VIMS pixel response function is variable within a pixel, unresolved objects like stars cannot be used with sufficient accuracy. Therefore, the only practical avenue that remains involves the use of known spectra of Saturn's icy satellites and rings, Saturn itself, Jupiter and Titan. Using a cross correlation of the spectra of the various objects, we were able to ascertain in general which "bumps and wiggles" in the response function were instrument related, and which were real features in the spectra of the various objects.

Furthermore, because the reflection spectra of solar-systems objects can be strong functions of their illumination geometry, the spectra of some objects were analyzed as a function of phase angle. For example, high-phase observations of Saturn's D and F-rings are expected to be dominated by diffraction, with muted spectral signatures of water ice, except near the water-ice vibrational fundamentals, where the real index of refraction becomes close to 1.0. The derived, relative-multiplier

vector for 2004.0 is shown in Figure 7.

VIMS has order-sorting filter gaps near 1.65, 3, and 3.9 microns (the upward spike in Figure 7), and they do not shift with time because they are fixed with respect to the detector array, whereas the spectrum of an object projected onto the detector array changes with time, and thus all other structure in spectral measurements does change in the IR channel of VIMS. The sampled wavelengths of the visible channel do not shift, thus its ground calibration is sufficient for calibration of the visible-channel data. The VIMS-IR multiplier vector (excluding the filter gap transmission) from Figure 7 was cubic-spline interpolated to the wavelength set derived for each year and given in Table 1. We then applied the effects of the filter-gap transmission.

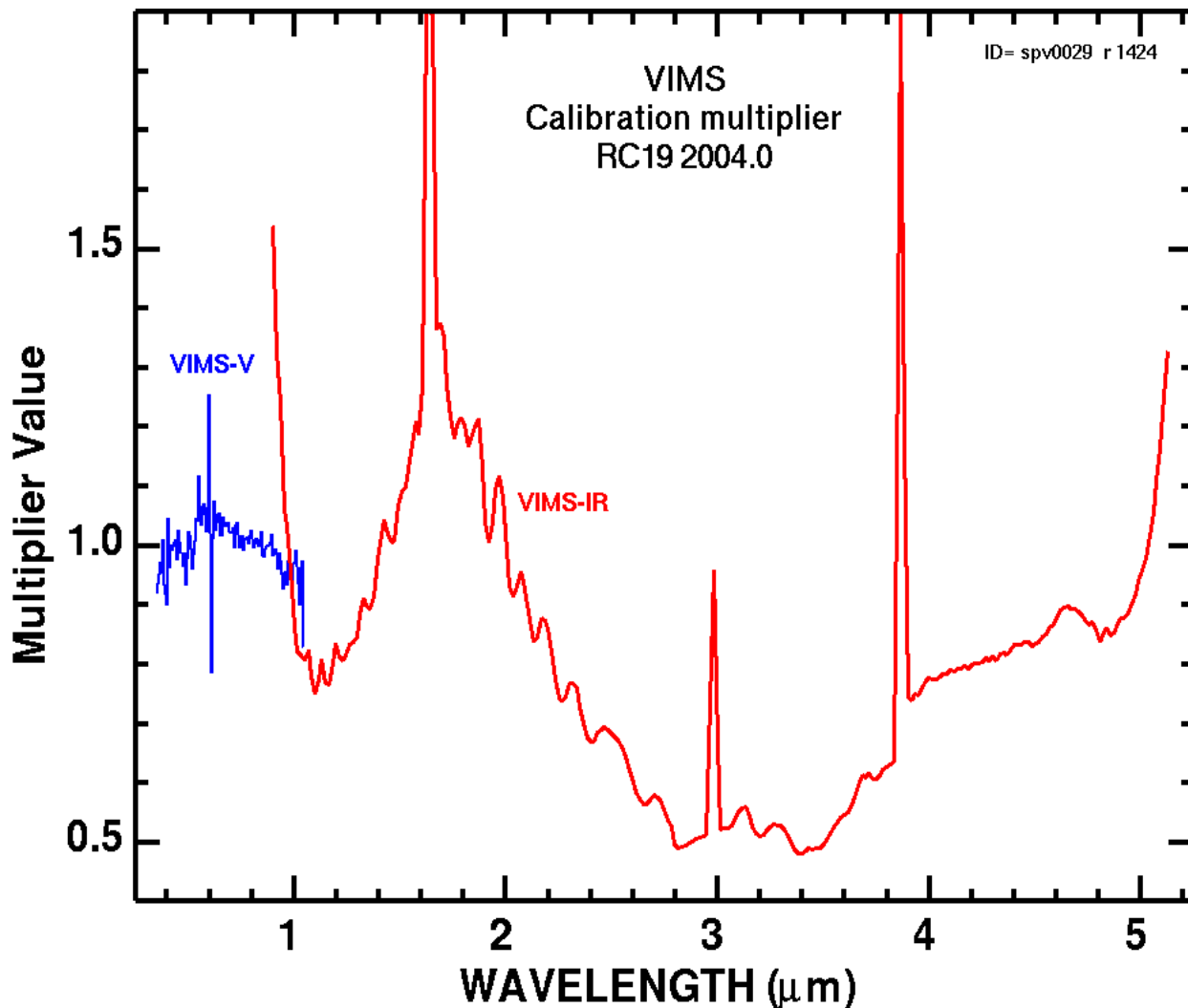


**Figure 7.** The relative calibration multiplier set for year 2004.0, used in Equation 4. The vector is resampled with time as described in the text.

The results of the new calibration are illustrated in Figure 8. The RC17 calibration, which does not take into account the effects of shifting wavelengths shows increasing ringing (compare The D-ring 2006 RC 17 with F-ring 2015 RC17 spectra). The new RC19 calibration, which tracks the effects of the shifting wavelength sets, eliminates the ringing problems.

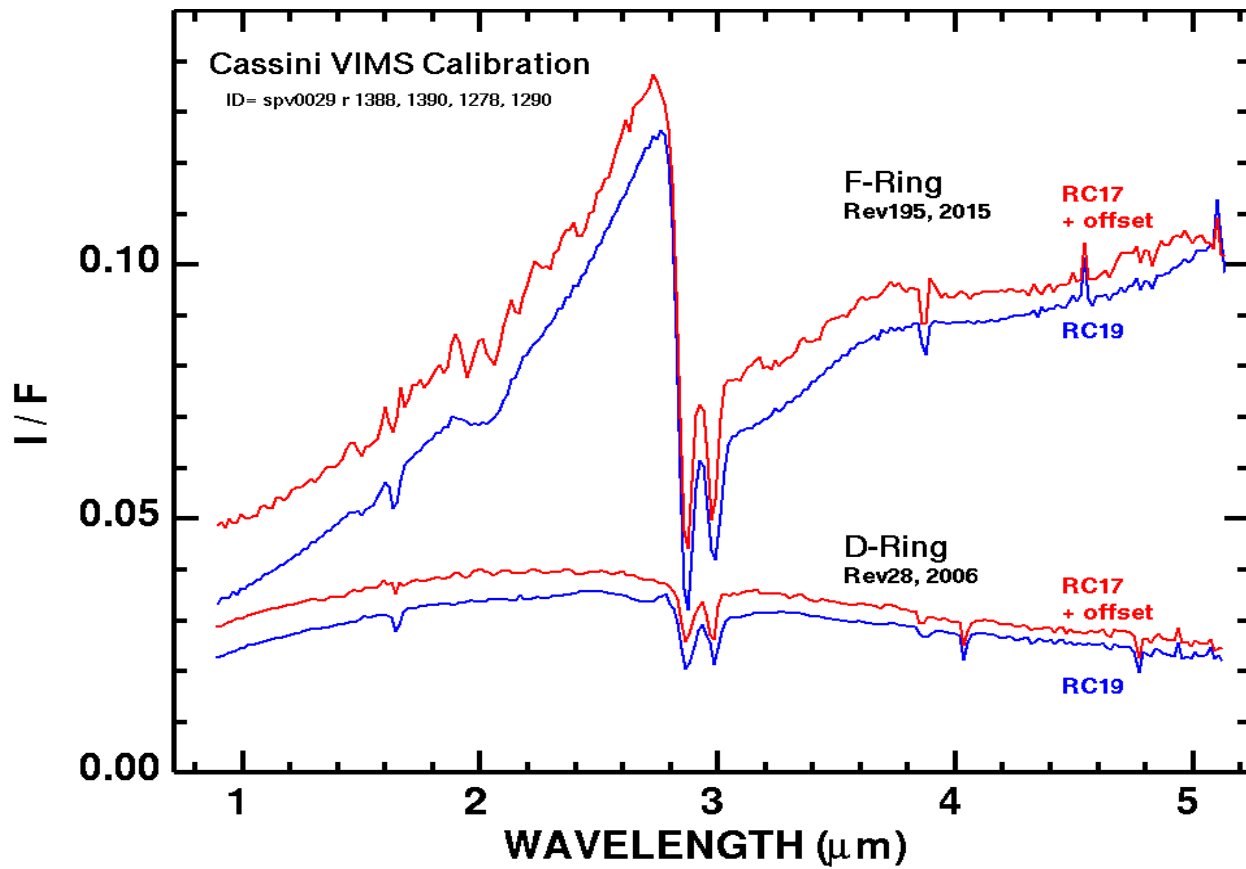


**Figure 8.** Example VIMS spectra using RC17 which was constant with time, and the new RC19 method described here.

## Application/implementation of the time-dependent transfer functions to calibration of data

Calibration of VIMS uses equation 3, above. The value of B from equation 2 is computed by selecting the wavelengths and FWHM for the time of the observation, and MKS units as follows.

$$\Omega = 2.5 \times 10^{-7} \text{ steradian.}$$

$$c = 2.998 \times 10^8 \text{ m/s.}$$

$$A = 0.00961 \text{ m}^2 \text{ (VIS), } 0.001588 \text{ m}^2 \text{ (IR).}$$

$$h = 6.626 \times 10^{-34} \text{ J-s (= W s}^2\text{).}$$

$\lambda$  = wavelength in meters (ascii listings are in microns. So divide by 1000.0).

$\Delta\lambda$  = FWHM in microns.

ASCII listing of the value of B for each VIMS channel is given in the Appendix.

In equation 3,

$$(4a) C_{\text{VIS}} = 29554. * \text{ calibration multiplier set from the appendix / (t * gain),}$$

$$(4b) C_{\text{IR}} = 8112. * \text{ calibration multiplier set from the appendix / (t * gain),}$$

the calibration multiplier set is one of the files with a name of

vims.calibration.multiplier.RC19-20NN.N.txt

where 20NN.N is the year. The constants in 4a and 4b apply to both standard and high resolution modes. Almost all VIMS observations have been carried out with gain = 1.

The Thompson *et al.* (2015) solar spectra convolved to VIMS are also given in the Appendix for each wavelength and calibration multiplier set.

The resulting units from equation 3 are dimensionless (I/F). To get to radiance, multiply by the solar spectrum. The supplied VIMS-convolved solar spectra are in units of Watts / m<sup>2</sup> / micron.

### Remaining Issues

No further analysis will be carried out by the VIMS Team after after this report. There are differences in the calibration that remain unresolved between RC19 and the earlier RC17. Remaining issues and uncertainties include the following.

1) The dip and rise near 2.6-2.9 microns may or may not be real (Figures 9, 10). The structure in this spectral region for the D-ring high phase observation is compared to spectra of Titan. The difference in the RC17 versus RC19 changes the intensities in the Titan windows in the 2.7 and 2.8 micron regions by about 5%. Which version is correct is not certain, though models suggest the RC17 is more correct at these wavelengths. However, the RC19 calibration may be showing a structure from another compound.

2) The feature near 3 microns is on the edge of the order sorting filter gap and may or may not be real. If real the feature is most likely due to an N-H stretch (e.g. ammonia or ammonium compound). Other space-based spectra through this spectral region are needed to resolve the issue.

3) The filter gap transmission around 1.65 and 3.9 microns may need adjustment.

4) The dip seen in Figure 9, top few spectra, between 4.5 and 5.1 microns may not be real. Or perhaps there is a rise between  $\sim 4.2$  and  $\sim 4.7$  microns that may not be real. This is less than a 5% effect.

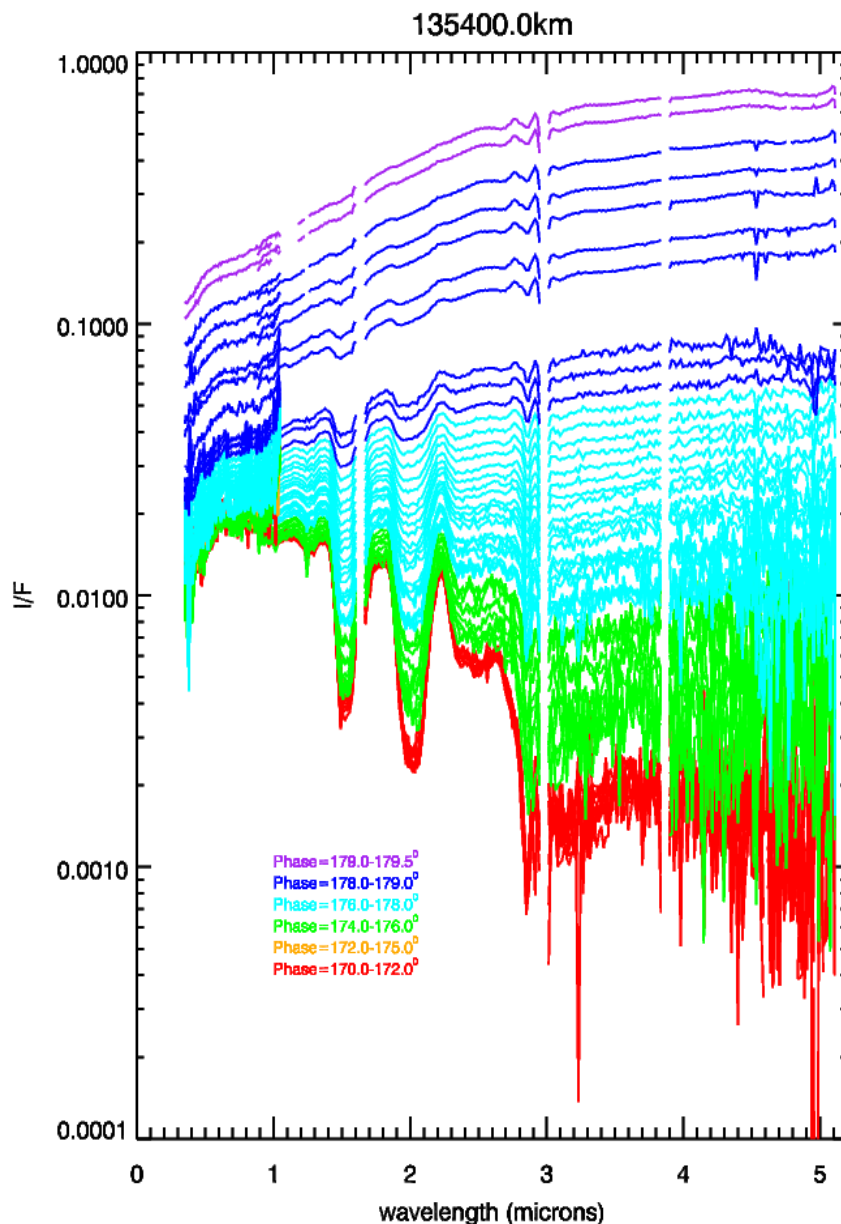


**Figure 9.** VIMS spectra of a region in the middle A ring derived from HIPHASE observations in Revs 263, 264 and 271. Each curve gives the average spectrum from all pixels within 25 cubes which observed the rings within a range of 0.1 degrees of phase angle and 100 km of 135,400 km. Note the decrease in H<sub>2</sub>O ice band depths with increasing phase angles. The feature at 2.85 microns may be real and due to the minimum in the index of refraction in ice at that wavelength. The spectral structure short of that minimum is in question. The spectral structure in the visible around 0.5 microns shows similarity to the index of refraction of metallic iron.

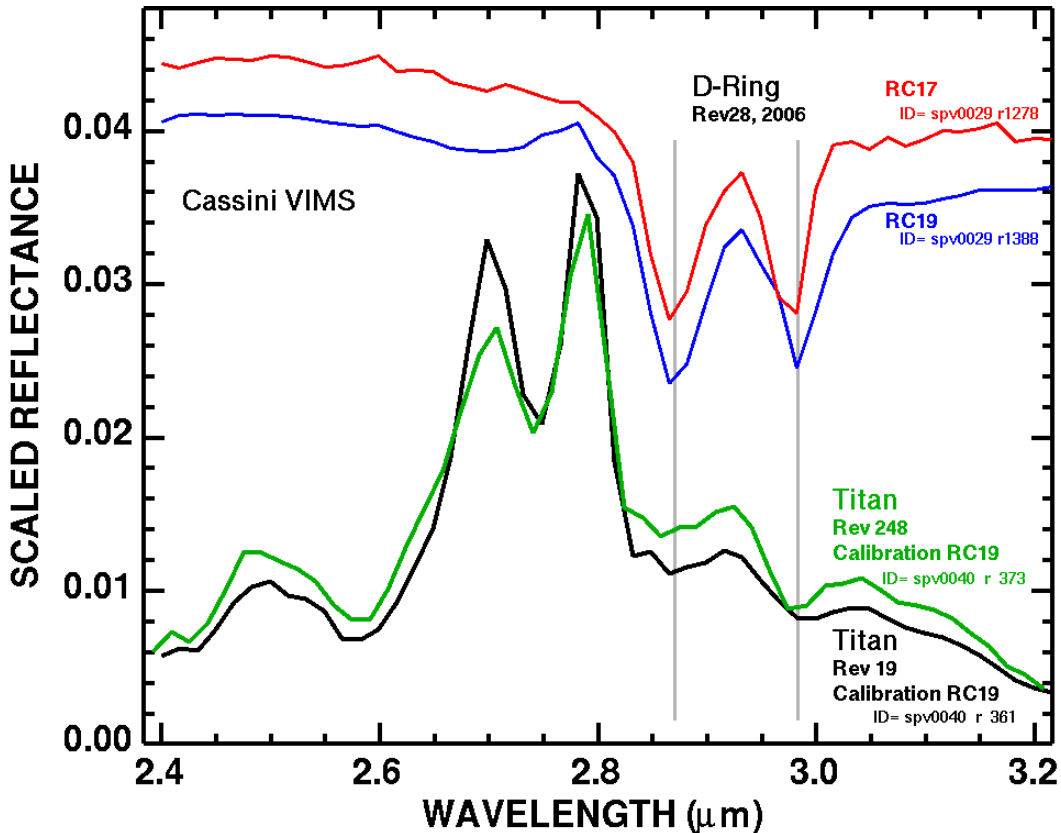


**Figure 10.** VIMS spectra of Titan and Dring at high phase are compared. Differences in the RC19 versus RC17 calibration changes the ratio of the intensities in the Titan 2.7 to 2.8-micron windows by about 5%. This ratio is sensitive to Titan’s surface composition. The spectral structure from about 2.62 to 2.82 microns is uncertain at about the 5% level. The 2.95 to 3.0-micron spectral structure is located at a VIMS order-sorting filter change so has some uncertainty. If real it could indicate the presence of  $\text{NH}_3$ . The 2.85-micron spectral feature in the D-ring spectra is real and is due to the minimum in the  $\text{H}_2\text{O}$  ice index of refraction.

## Appendices

A tar file, `vims-calibration+wavelengths-vs-time-files-rc19-2018.tar`, contains ascii listings of the wavelengths, calibration multiplier, the computed B values (equation 2), and the VIMS-convolved solar spectrum as a function of time. The time increment is 1 year centered mid year. The VIMS wavelength shift is small enough that this granularity is sufficient for most applications, as the shift between these calibrations is less than 0.05 channel.

## Conclusions

The VIMS wavelengths are shifting small amounts per year (less than 0.1 channel) during the Saturn orbital tour and larger amounts during the Jupiter fly-by, necessitating the need for a time-dependent calibration. We have derived a new methodology that tracks this change and produces significantly better spectra with lower noise and lower artifacts. This new calibration should enable greater

confidence in observed spectral features, leading to detection of lower abundance components and therefore new and better science.

**Table 1**

Time	Shift (nm)	Add to standard Wavelength set: (microns)	Change in interval		
			- to +		
			(nm)		
1999.6	-25.8	-0.0258		0.0	
2000.064	-25.8	-0.0258	0.0	0.5	
2000.350	-24.8	-0.0248	0.5	0.5	
2000.630	-23.8	-0.0238	0.5	0.5	
2000.695	-22.8	-0.0228	0.5	0.5	
2000.743	-21.8	-0.0218	0.5	0.5	
2000.776	-20.8	-0.0208	0.5	0.5	
2000.805	-19.8	-0.0198	0.5	0.5	
2000.824	-18.8	-0.0188	0.5	0.5	
2000.842	-17.8	-0.0178	0.5	0.5	
2000.856	-16.8	-0.0168	0.5	0.5	
2000.868	-15.8	-0.0158	0.5	0.5	
2000.878	-14.8	-0.0148	0.5	0.5	
2000.884	-13.8	-0.0138	0.5	0.5	
2000.894	-12.8	-0.0128	0.5	0.5	
2000.903	-11.8	-0.0118	0.5	0.5	
2000.911	-10.8	-0.0108	0.5	0.5	
2000.918	-9.8	-0.0098	0.5	0.5	
2000.925	-8.8	-0.0088	0.5	0.5	
2000.931	-7.8	-0.0078	0.5	0.5	
2000.936	-6.8	-0.0068	0.5	0.5	
2000.942	-5.8	-0.0058	0.5	0.5	
2000.947	-4.8	-0.0048	0.5	0.5	
2000.952	-3.8	-0.0038	0.5	0.5	
2000.956	-2.8	-0.0028	0.5	0.5	
2000.961	-1.8	-0.0018	0.5	0.5	
2001.12	-0.8	-0.0008	0.5	0.5	
2001.30	0.2	0.0002	0.3	0.5	
2001.50	1.2	0.0012	0.5	0.6	

2002.0-2005.0	0.0	0.0000	0.6	0.2	"Standard wavelengths"
2005.5	0.4	0.0004	0.2	0.4	
2006.0	1.1	0.0011	0.4	0.4	
2006.5	1.9	0.0019	0.4	0.4	
2007.0	2.6	0.0026	0.4	0.4	
2007.5	3.4	0.0034	0.4	0.4	
2008.0	4.1	0.0041	0.4	0.4	
2008.5	4.9	0.0049	0.4	0.4	
2009.0	5.6	0.0056	0.4	0.2	
2009.5	6.0	0.0060	0.2	0.0	
2010.0	6.0	0.0060	0.0	0.0	
2010.5	6.0	0.0060	0.0	0.0	
2011.0	6.0	0.0060	0.0	0.0	
2011.5	7.0	0.0070	0.5	0.2	
2012.0	7.3	0.0073	0.2	0.2	
2012.5	7.7	0.0077	0.2	0.2	
2013.0	8.0	0.0080	0.2	0.2	
2013.5	8.4	0.0084	0.2	0.2	
2014.0	8.7	0.0087	0.2	0.2	
2014.3	9.1	0.0091	0.2	0.0	change from 2016 RC19 in 4/20/2017 starts here
2014.5	9.1	0.0091	0.0	0.1	
2015.0	9.2	0.0092	0.1	0.1	
2015.5	9.3	0.0093	0.1	0.1	
2016.0	9.4	0.0094	0.1	0.1	
2016.5	9.5	0.0095	0.1	0.1	
2017.0	9.6	0.0096	0.1	0.1	
2017.5	9.7	0.0097	0.1	0.1	
2017.8	9.8	0.0098	0.1		

**Table 2**

VIMS Standard Wavelengths (2004.0)

	Standard wavelength (microns)	FWHM (microns)
1	0.350540	0.007368
2	0.358950	0.007368
3	0.366290	0.007368
4	0.373220	0.007368
5	0.379490	0.007368
6	0.387900	0.007368
7	0.395180	0.007368
8	0.402520	0.007368
9	0.409550	0.007368
10	0.417310	0.007368
11	0.424360	0.007368
12	0.431840	0.007368
13	0.439190	0.007368
14	0.446520	0.007368
15	0.453720	0.007368
16	0.461630	0.007368
17	0.468410	0.007368
18	0.476220	0.007368
19	0.486290	0.007368
20	0.489670	0.007368
21	0.497770	0.007368
22	0.506280	0.007368
23	0.512220	0.007368
24	0.519630	0.007368
25	0.527660	0.007368
26	0.534160	0.007368
27	0.541560	0.007368
28	0.549540	0.007368
29	0.556140	0.007368
30	0.563530	0.007368
31	0.571310	0.007368
32	0.578100	0.007368
33	0.585480	0.007368
34	0.593120	0.007368
35	0.599380	0.007368
36	0.607570	0.007368
37	0.615050	0.007368
38	0.622070	0.007368
39	0.629400	0.007368
40	0.637040	0.007368
41	0.644080	0.007368
42	0.651420	0.007368

43	0.659100	0.007368
44	0.666090	0.007368
45	0.673420	0.007368
46	0.681020	0.007368
47	0.688030	0.007368
48	0.695350	0.007368
49	0.702880	0.007368
50	0.710000	0.007368
51	0.717330	0.007368
52	0.724840	0.007368
53	0.731980	0.007368
54	0.739300	0.007368
55	0.746760	0.007368
56	0.753960	0.007368
57	0.761280	0.007368
58	0.768740	0.007368
59	0.775950	0.007368
60	0.783280	0.007368
61	0.790720	0.007368
62	0.797930	0.007368
63	0.805220	0.007368
64	0.812620	0.007368
65	0.819890	0.007368
66	0.827210	0.007368
67	0.834630	0.007368
68	0.841900	0.007368
69	0.849220	0.007368
70	0.856630	0.007368
71	0.863910	0.007368
72	0.871220	0.007368
73	0.878630	0.007368
74	0.885890	0.007368
75	0.893860	0.007368
76	0.900320	0.007368
77	0.907870	0.007368
78	0.915180	0.007368
79	0.922540	0.007368
80	0.929830	0.007368
81	0.937130	0.007368
82	0.944450	0.007368
83	0.951770	0.007368
84	0.959070	0.007368
85	0.966380	0.007368
86	0.973820	0.007368
87	0.981000	0.007368
88	0.988830	0.007368
89	0.995880	0.007368
90	1.002950	0.007368
91	1.010050	0.007368

92	1.016950	0.007368	
93	1.024710	0.007368	
94	1.031950	0.007368	
95	1.038650	0.007368	
96	1.045980	0.012480	End of VIS channel
97	0.884210	0.012878	
98	0.900753	0.012767	
99	0.916924	0.012507	
100	0.933078	0.013169	
101	0.949803	0.012869	
102	0.965683	0.012728	
103	0.982262	0.013370	
104	0.998820	0.012790	
105	1.014790	0.012748	
106	1.031320	0.013186	
107	1.047550	0.012847	
108	1.065410	0.013136	
109	1.081830	0.013063	
110	1.098060	0.012686	
111	1.113960	0.012828	
112	1.130240	0.013111	
113	1.146950	0.013322	
114	1.163700	0.013266	
115	1.179960	0.012968	
116	1.196220	0.013018	
117	1.212460	0.012921	
118	1.228590	0.013031	
119	1.244920	0.013401	
120	1.261660	0.013631	
121	1.278130	0.013372	
122	1.294820	0.013121	
123	1.310910	0.013101	
124	1.326950	0.013146	
125	1.343240	0.013389	
126	1.359520	0.013663	
127	1.376950	0.013366	
128	1.393260	0.012821	
129	1.409400	0.013147	
130	1.425570	0.013137	
131	1.441840	0.013216	
132	1.458410	0.013480	
133	1.475140	0.013610	
134	1.491690	0.013066	
135	1.507940	0.013063	
136	1.524210	0.012992	
137	1.540350	0.013059	
138	1.556740	0.013388	
139	1.573610	0.014011	
140	1.590180	0.013901	

141	1.602280	0.008457	order-sorting filter change
142	1.625230	0.032000	order-sorting filter change
143	1.641600	0.009862	order-sorting filter change
144	1.655670	0.013304	
145	1.672380	0.013532	
146	1.689010	0.013253	
147	1.705360	0.013300	
148	1.721750	0.013068	
149	1.738020	0.013084	
150	1.754360	0.013155	
151	1.771050	0.013455	
152	1.787710	0.013080	
153	1.804010	0.013090	
154	1.820040	0.012902	
155	1.836160	0.012985	
156	1.852880	0.013531	
157	1.869330	0.012939	
158	1.886790	0.012600	
159	1.902610	0.013058	
160	1.919160	0.013059	
161	1.935450	0.013127	
162	1.951910	0.013498	
163	1.968710	0.013615	
164	1.985310	0.013293	
165	2.001670	0.013209	
166	2.017810	0.013294	
167	2.034240	0.013415	
168	2.050910	0.013889	
169	2.067570	0.013472	
170	2.084000	0.013579	
171	2.100340	0.013428	
172	2.116670	0.013719	
173	2.133370	0.013943	
174	2.150180	0.013787	
175	2.166520	0.013547	
176	2.182880	0.013600	
177	2.199200	0.013571	
178	2.215910	0.014009	
179	2.232820	0.013918	
180	2.249520	0.013700	
181	2.266220	0.013600	
182	2.282380	0.014012	
183	2.299210	0.013974	
184	2.316120	0.014211	
185	2.333250	0.014287	
186	2.350430	0.014407	
187	2.367650	0.014286	
188	2.384720	0.014294	
189	2.401560	0.014079	

190	2.418200	0.013921	
191	2.434710	0.013829	
192	2.450970	0.013748	
193	2.467230	0.013784	
194	2.483600	0.014044	
195	2.500020	0.014293	
196	2.516590	0.014306	
197	2.532920	0.013704	
198	2.549160	0.013918	
199	2.564370	0.011963	
200	2.581760	0.013610	
201	2.598070	0.014726	
202	2.615080	0.012722	
203	2.630000	0.011283	
204	2.646500	0.013711	
205	2.661460	0.012674	
206	2.680850	0.016119	
207	2.696200	0.014697	
208	2.712050	0.015964	
209	2.732700	0.012786	
210	2.747700	0.018701	
211	2.763050	0.016296	
212	2.781180	0.013689	
213	2.798890	0.014400	
214	2.816060	0.015083	
215	2.832470	0.014680	
216	2.849540	0.014842	
217	2.866090	0.015667	
218	2.882420	0.015534	
219	2.898780	0.015325	
220	2.915400	0.015088	
221	2.931430	0.015720	
222	2.947260	0.015350	
223	2.963270	0.015716	order-sorting filter change
224	2.977200	0.015512	order-sorting filter change (~30% transmission)
225	3.000720	0.012919	order-sorting filter change
226	3.013820	0.015570	
227	3.029700	0.015398	
228	3.048060	0.014922	
229	3.064460	0.015466	
230	3.080360	0.015882	
231	3.096890	0.015851	
232	3.112130	0.015753	
233	3.129620	0.016580	
234	3.146670	0.015851	
235	3.163040	0.016127	
236	3.179740	0.016115	
237	3.197080	0.015685	
238	3.213640	0.015830	

239	3.231500	0.016740	
240	3.248060	0.017771	
241	3.265610	0.016161	
242	3.282980	0.016285	
243	3.299460	0.016286	
244	3.316190	0.015816	
245	3.333380	0.015203	
246	3.349810	0.016500	
247	3.365640	0.015590	
248	3.381830	0.015717	
249	3.398720	0.016471	
250	3.415460	0.016457	
251	3.431780	0.016343	
252	3.448740	0.015852	
253	3.464750	0.015634	
254	3.481370	0.015608	
255	3.497950	0.015779	
256	3.512840	0.016141	
257	3.530150	0.015057	
258	3.546640	0.016643	
259	3.562740	0.016735	
260	3.580340	0.016474	
261	3.596100	0.017033	
262	3.613870	0.020159	
263	3.630850	0.018293	
264	3.648530	0.017622	
265	3.665220	0.018895	
266	3.682830	0.018505	
267	3.699530	0.019496	
268	3.717430	0.018635	
269	3.734390	0.019045	
270	3.751030	0.019296	
271	3.767630	0.017966	
272	3.784440	0.019006	
273	3.800830	0.018599	
274	3.817420	0.018210	
275	3.834720	0.019856	
276	3.851410	0.018125	
277	3.861840	0.015574	order-sorting filter change
278	3.881670	0.023959	order-sorting filter change
279	3.898590	0.020270	
280	3.914780	0.021217	
281	3.930690	0.020631	
282	3.947620	0.019721	
283	3.963750	0.020799	
284	3.980150	0.021142	
285	3.996720	0.021846	
286	4.012800	0.021142	
287	4.029440	0.021531	

288	4.047300	0.021598	
289	4.062950	0.022566	
290	4.080861	0.021479	
291	4.097430	0.022433	
292	4.114500	0.022013	
293	4.131830	0.022290	
294	4.148830	0.022294	
295	4.166440	0.020424	
296	4.183199	0.021180	
297	4.200100	0.019057	
298	4.217000	0.017383	
299	4.233700	0.022866	
300	4.250500	0.021600	
301	4.267300	0.021600	
302	4.284000	0.021600	
303	4.300600	0.021600	
304	4.317101	0.021600	
305	4.333600	0.021600	
306	4.350200	0.019916	
307	4.366500	0.021335	
308	4.382900	0.020260	
309	4.397930	0.019563	
310	4.415370	0.021034	
311	4.431720	0.019802	
312	4.447720	0.019867	
313	4.465730	0.019735	
314	4.482400	0.019931	
315	4.499511	0.021189	
316	4.515910	0.020529	
317	4.533790	0.019303	
318	4.551870	0.019921	
319	4.567970	0.020376	
320	4.585560	0.020113	
321	4.602900	0.019105	
322	4.620100	0.020267	
323	4.636150	0.017409	
324	4.654160	0.019612	
325	4.670340	0.018281	
326	4.687210	0.019814	
327	4.702900	0.017902	
328	4.719561	0.020080	
329	4.737060	0.018831	
330	4.753510	0.018017	
331	4.770310	0.015955	hot pixel
332	4.786730	0.018821	
333	4.803490	0.017274	
334	4.819521	0.018179	
335	4.835771	0.018545	
336	4.852920	0.018106	

337	4.869401	0.018799	
338	4.885530	0.019556	
339	4.902650	0.018114	
340	4.919831	0.018570	
341	4.936851	0.017740	slightly noisier (1.5x at low signal)
342	4.953890	0.018779	
343	4.971780	0.018266	
344	4.988960	0.020001	
345	5.005760	0.018402	
346	5.022400	0.018621	
347	5.040781	0.016783	
348	5.057340	0.019510	
349	5.074020	0.017953	
350	5.091060	0.020883	slightly noisier (2x at low signal)
351	5.106800	0.015704	
352	5.122500	0.016	

## References

- Al-Jumaily, G.A., E. Miller, and N. Raof, 1991, C/C VIMS Filter requirements, JPL VIMS Design File Memorandum, 6-25-1991.
- Brown, R.H., Baines, K.H., Bellucci, J.P., Bibring, B.J., Buratti, E., Bussoletti, F., Capaccioni, P., Cerroni, P., Clark, R.N., Coradini, D.P., Cruikshank, P., Drossart, Y., Formisano, R., Jaumann, Y., Langevin, D.J., Matson, T.R., 2005, The Cassini visual and infrared mapping spectrometer investigation: *Space Science Reviews*, **115 (1-4)**, 111-168.
- Clark, R. N., D. P. Cruikshank, R. Jaumann, R. H. Brown, K. Stephan, C. M. Dalle Ore, K. E. Livo, N. Pearson, J. M. Curchin, T. M. Hoefen, B. J. Buratti, G. Filacchione, K. H. Baines, and P. D. Nicholson, 2012, The Composition of Iapetus: Mapping Results from Cassini VIMS, *Icarus*, **218**, 831-860.
- Clark, R. N., R. H. Brown, and D. M. Lytle, 2016, The VIMS Wavelength and Radiometric Calibration, *NASA Planetary Data System*, [The Planetary Atmospheres Node](#), 23p.
- Cruikshank, D. P., A. W. Meyerb and, R. H. Brown and, R. N. Clark, R. Jaumann, K. Stephan, C. A. Hibbitts, S. A. Sandford, R. M.E. Mastrapa, G. Filacchione, C. M. Dalle Ore, P. D. Nicholson, B. J. Buratti, T. B. McCord, R. M. Nelson, J. B. Dalton, K. H. B., and D. L. Matson, 2010, Carbon dioxide on the satellites of Saturn: Results from the Cassini VIMS investigation and revisions to the VIMS wavelength scale, *Icarus*, **206**, 561–572, doi:10.1016/j.icarus.2009.07.012 .
- McCord, T. B., Brown, R., Baines, K., Bellucci, G., Bibring, J.-P., Buratti, B., Capaccioni, F., Cerroni, P., Clark, R.N., Coradini, A., Cruikshank, D., Drossar, P., Formisano, V., Jaumann, R., Langevin, Y., Matson, D., Mennella, V., Nelson, R., Nicholson, P., Sicardy, B., Sotin, C., Hansen, G., Hibbitts, C., 2004, Cassini VIMS observations of the Galilean satellites, including the VIMS calibration procedure: *Icarus*, Vol. 172, p. 104-126.
- Miller, Edward A., Gail Klein, David W. Juergens, Kenneth Mehaffey, Jeffrey M. Oseas, Ramon A. Garcia, Anthony Giandomenico, Robert E. Irigoyen, Roger Hickok, David Rosing, Harold R. Sobel, Carl F. Bruce, Jr., Enrico Flamini, Romeo DeVidi, Francis M. Reininger, Michele Dami, Alain Soufflot, Yves Langevin, Gerard Huntzinger, 1996, The Visual and Infrared Mapping Spectrometer for Cassini , *Proc. SPIE* **2803**, *Cassini/Huygens: A Mission to the Saturnian Systems*, 206-220 (October 7, 1996), doi: 10.1117/12.253421 .
- Thompson, D. R., F. C. Seidel, B. C. Gao, M. M. Gierach, R. O. Green, R. M. Kudela, and P. Mouroulis , 2015, Optimizing irradiance estimates for coastal and inland water imaging spectroscopy, *Geophys. Res. Lett.*, **42**, 4116–4123, doi:10.1002/2015GL063287.